### **CHEMISTRY**

# High pressure-derived nonsymmetrical [Cu<sub>2</sub>O]<sup>2+</sup> core for room-temperature methane hydroxylation

Peter E. VanNatta<sup>1</sup>, Cynthia M. Archambault<sup>1</sup>, Sicheng Wang<sup>1</sup>, Tengteng Lyu<sup>1</sup>, Jack D'Amelio<sup>2</sup>, Noah J. Martell<sup>3</sup>, Scott K. Watson<sup>1</sup>, Kunyu Wang<sup>4</sup>, Zhenxian Liu<sup>5</sup>, Matthew T. Kieber-Emmons<sup>6</sup>, Hao Yan<sup>1</sup>\*

Nonsymmetrical oxygen-bridged binuclear copper centers have been proposed and modeled as intermediates and transition states in several C—H oxidation pathways, leading to the postulation that structural dissymmetry enhances the reactivity of the bridging oxygen. However, experimentally characterizing the structure and reactivity of these transient species is remarkably challenging. Here, we report the high-pressure synthesis of a metastable nonsymmetrical dicopper- $\mu$ -oxo compound with exceptional reactivity toward the mono-oxygenation of aliphatic C—H bonds. The nonequivalent coordination environment of copper stabilizes localized mixed valency and greatly enhances the hydrogen atom abstraction activity of the bridging oxygen, enabling room-temperature hydroxylation of methane under pressure. These findings highlight the role of dissymmetry in the reactivity of binuclear copper centers and demonstrate precise control of molecular structures by mechanical means.

Copyright © 2024 me
Authors, some rights
reserved; exclusive
licensee American
Association for the
Advancement of
Science. No claim to
original U.S.
Government Works.
Distributed under a
Creative Commons
Attribution
NonCommercial
License 4.0 (CC BY-NC).

### **INTRODUCTION**

Nonsymmetrical coupled binuclear copper (CBC) centers have been proposed in catalytic cycles involving type III copper proteins (1-3), e.g., tyrosinase (4-5) and catechol oxidase (6-8), as well as copperexchanged zeolites (9-11), for the mono-oxygenation of C-H and O—H bonds. For example, the transition state for methane hydroxylation in Cu-ZSM-5, modeled by density functional theory (DFT), is a distorted dicopper- $\mu$ -oxo,  $[Cu_2O]^{2+}$ , core with the bridging oxygen strongly bound to one copper; the dissymmetry renders the oxygen with radical characteristics, lowering the activation barrier for the rate-limiting hydrogen atom abstraction (HAA) step (9). Similarly, a nonsymmetrical dicopper-μ-superoxo (Cu<sub>2</sub>O<sub>2</sub>) transition state is modeled by DFT for the HAA from phenolic O—H by catechol oxidase (6). These models suggest that dissymmetry of the CBC enhances the reactivity of the bridging oxygen species. This postulation is indeed supported by the experimentally characterized nonsymmetrical distorted  $[Cu_2O]^{2+}$  active site ( $\angle Cu-O-Cu = 99.6^{\circ}$ ) in Cu<sub>2</sub>@C<sub>3</sub>N<sub>4</sub> for selective methane hydroxylation (12). However, mimicking the nonsymmetrical structure and the resultant reactivity in molecular systems remains an outstanding challenge. Most molecular compounds bearing the CBC motif are symmetrical (13–17), and the few examples of nonsymmetrical CBCs have not demonstrated enhanced reactivity related to the structural dissymmetry (18–20).

We use hydrostatic pressure generated in a diamond anvil cell (DAC) and in situ spectroscopy (21, 22) to traverse a unique reaction path, culminating in a metastable nonsymmetrical dicopper- $\mu$ -oxo complex with unprecedented C—H mono-oxygenation reactivity. The precursor, {[(TMPA)Cu<sup>(II)</sup>]<sub>2</sub>( $\mu$ -OH)}<sup>3+</sup> (1) features two chemically equivalent Cu(II) supported by tris(2-pyridylmethyl)amine (TMPA) ligands and bridged by a hydroxo ligand (fig. S1 and tables S1 and S2).

<sup>1</sup>Department of Chemistry, University of North Texas, Denton, TX 76205, USA. <sup>2</sup>Department of Chemistry, University of Illinois at Urbana-Champaign, Urbana, IL 61801, USA. <sup>3</sup>Department of Chemistry, Iowa State University, Ames, IA 50011, USA. <sup>4</sup>Department of Chemistry, Texas A&M University, College Station, TX 77843, USA. <sup>5</sup>Department of Physics, University of Illinois Chicago, Chicago, IL 60607, USA. <sup>6</sup>Department of Chemistry, Cedar Crest College, Allentown, PA 18104, USA. \*Corresponding author. Email: hao.yan@unt.edu

1 and its conjugate base,  $\{[(TMPA)Cu^{(II)}]_2(\mu-O)\}^{2+}$ , have been extensively studied in the context of C—H mono-oxygenation (23, 24).

### **RESULTS**

### Pressure-induced proton transfer

We first demonstrate that pressure drives an intramolecular proton transfer in 1 (Fig. 1A). Single crystal of 1 shows a color change from blue to green upon hydrostatic compression to 8.5 gigapascal (GPa; Fig. 1B). In situ Raman spectroscopy reveals the O—H stretching mode,  $\nu$ (O–H), blue shifts by <3 cm<sup>-1</sup> from ambient pressure to 6.4 GPa (Fig. 1C and fig. S2), in contrast to the large, >80 cm<sup>-1</sup>, blue shift of the C-H stretching modes in the same pressure range (Fig. 1D). The  $\nu$ (O–H) band vanishes at 8.8 GPa, concurrent with the color change and indicating O—H bond breaking. Coincident with the color change and vanishing  $\nu(O-H)$ , the pyridyl (Py) breathing modes at 1570 and 1606 cm<sup>-1</sup> are obscured by a peak at 1628 cm<sup>-1</sup> (Fig. 1E). This feature is assigned to the breathing mode of pyridinium (PyH<sup>+</sup>), supported by literature (25) and DFT (Fig. 1F, fig. S3, and see discussion below). Deuterated 1, i.e.,  $\{[(TMPA)Cu^{(II)}]_2(\mu-OD)\}^{3+}$ , shows the same spectral change at substantially higher pressure, 12 GPa (fig. S4). We attribute the delayed transition to the O-D versus O-H kinetic isotope effect (26). Last, the symmetric and anti-symmetric Cu-O stretching modes,  $\nu_s$ (Cu-O-Cu) and  $\nu_{as}$ (Cu–O–Cu), are identified by <sup>18</sup>O labeling, DFT, and pressuredependent resonance enhancement (figs. S5 to S7). Both modes persist at 8.8 GPa (Fig. 1G), indicating the intactness of the Cu—O—Cu core after the transition. These Raman features are evident of an intramolecular proton transfer from the bridging hydroxo ligand to a dissociated pyridyl arm of the TMPA at 8.8 GPa. The color and spectral changes persist upon releasing the pressure, yet gradually relapse to the initial "blue state" over the course of a few days at room temperature in inert atmosphere. These observations indicate the formation of a new metastable compound, 2, best described as {[(TMPA) Cu] $-(\mu$ -O) $-[Cu(TMPAH^+)]^{3+}$  (Fig. 1A, right).

DFT modeling of **2** indeed affords a stable structure without external stress or constraint (Fig. 1H, fig. S8, and table S3). DFT is carried out using the B3LYP functional and a mixed Pople basis set

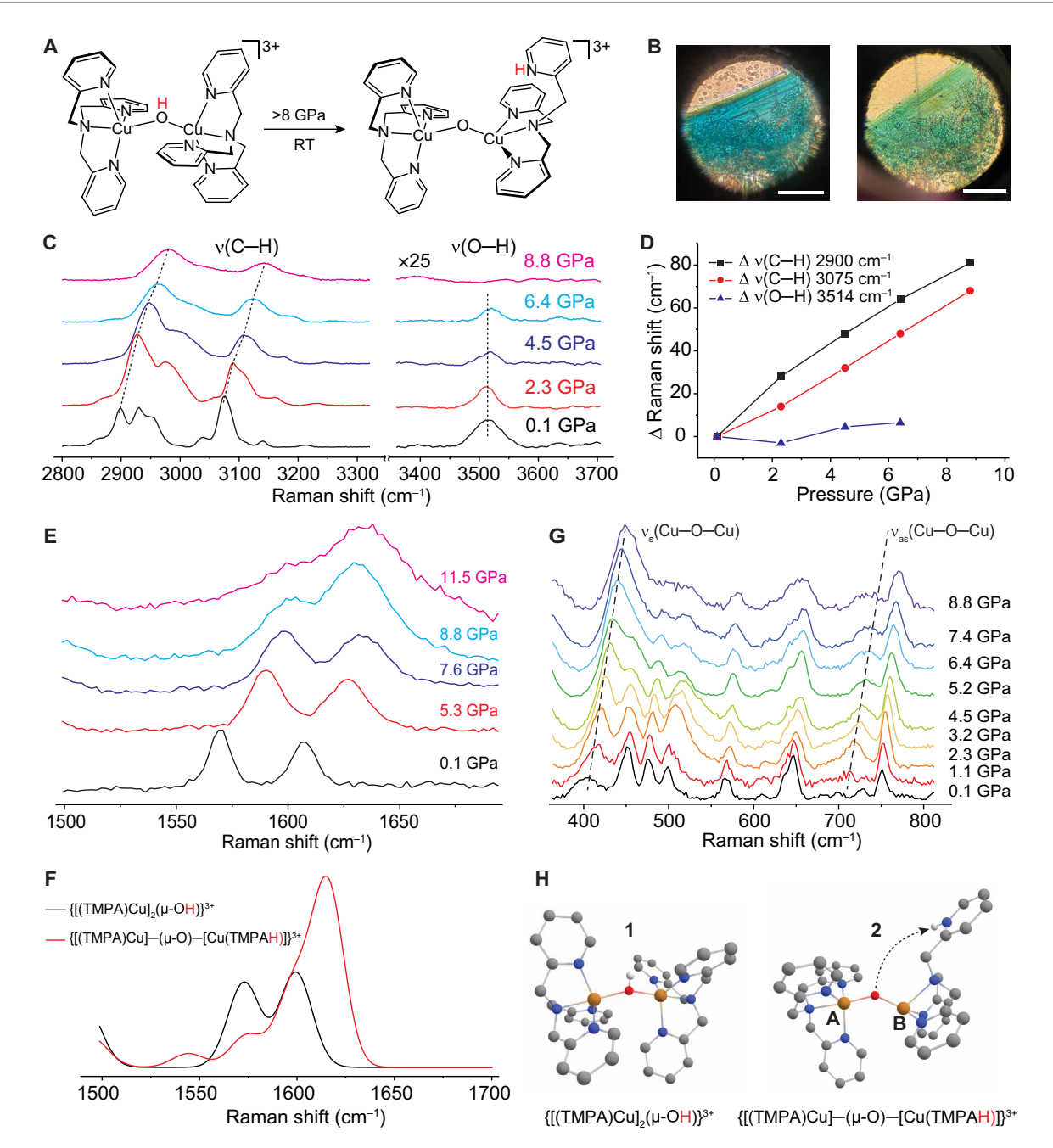


Fig. 1. High-pressure synthesis of 2. (A) Schematic of reaction. The transferred proton is highlighted in red. (B) Micrograph images of the crystal in the DAC at 0.1 (left) and 9.9 (right) GPa. Scale bars, 200  $\mu$ m. (C) Raman spectra in the  $\nu$ (C—H) and  $\nu$ (O—H) regions. (D) Relative shifts of  $\nu$ (C—H) and  $\nu$ (O—H) with pressure. (E) Raman spectra in the pyridyl/pyridinium ring breathing region. (F) DFT-computed Raman spectra of 1 and 2. (G) Raman spectra in the  $\nu$ (Cu—O—Cu) region. (H) DFT-optimized structures of 1 and 2. Copper, oxygen, nitrogen, carbon, and hydrogen atoms are represented by brown, red, blue, gray, and white spheres, respectively. Hydrogens on the TMPA liquid are omitted for clarity. The dashed arrow denotes the direction of proton transfer.

consisting of 6-311g\* on the Cu, N, and O and 6-31g on C and H, which has been shown to accurately determine the thermodynamics of this system (24). Simulated Raman of 2 shows the characteristic pyridinium breathing mode (Fig. 1F), consistent with experimental observation.

Compound 2 shows several notable features. First, the two copper atoms that are chemically equivalent in 1 have different ligand

fields in **2**. The TMPA-bound Cu(A) has trigonal bipyramidal (TBP) coordination same as that in **1**. In contrast, the TMPAH<sup>+</sup>-bound Cu(B) resides in a heavily distorted 4-coordinate ligand field. Second, the Cu—O—Cu center shows a bond angle of 141°, distinct from the linear  $[Cu_2O]^{2+}$  core proposed for  $\{[(TMPA)Cu^{(II)}]_2(\mu-O)\}^{2+}$  in solution (23). Last, heating and laser irradiation decompose **1** without forming **2** (fig. S9).

# **Reaction mechanism**

We hypothesize that mechanical deformation of the [Cu<sub>2</sub>OH]<sup>3+</sup> core facilitates the proton transfer. To test this, we model the highpressure crystal structures of 1 using periodic DFT with the Perdew-Burke-Ernzerhof (PBE) functional (27) and plane-wave basis sets (Fig. 2A, fig. S10, and table S4). The molecular strain in 1 is anisotropic under hydrostatic pressure. The bond lengths (C-C, C-N, Cu-N, and Cu-O) show small, <0.1 Å, contraction from ambient pressure to 20 GPa (Fig. 2B and table S5). In contrast, the Cu-Cu distance decreases by 0.4 Å in the same pressure range. Accordingly, the ∠Cu—O—Cu angle decreases from 140° to 123° (Fig. 2C). Anisotropic deformation is critical for mechanochemical reactivity under isotropic compression (21). The O—H bond length changes less than 0.001 Å, consistent with the observed quasi-stationary  $\nu$ (O–H). The periodic DFT does not reproduce the  $1 \rightarrow 2$  transition due to negligence of the thermal activation and limited phase space searched by the local optimization algorithm (see Supplemental Materials and Methods).

To understand the correlation between Cu-O-Cu bending and the proton transfer, we model the  $[Cu_2OH]^{3+}$  core by DFT with a series of constrained Cu-Cu distances. This truncated model replicates the most crucial deformations of the periodic DFT-computed structures, including bending of  $\angle Cu-O-Cu$  and a slight decrease of the Cu-O distance (Fig. 2D and fig. S11). Fully relaxed  $[Cu_2OH]^{3+}$  has an antiferromagnetically coupled singlet ground state, stabilized by the superexchange interaction through the bridging oxygen, and a low-lying triplet state (fig. S12), consistent with 1 at ambient pressure in solution (23). We expect that as the  $\angle Cu-O-Cu$  decreases, the

singlet state is destabilized due to diminished overlap between Cu 3d and O 2p orbitals (1). A singlet-to-triplet crossover is observed as ∠Cu—O—Cu decreases from 138° to 135° (Cu···Cu distance from 3.5 to 3.45 Å) corresponding to the structure between 5 and 10 GPa from the periodic DFT. The net spin on oxygen increases substantially, from 0 at 140° ∠Cu—O—Cu (Cu···Cu distance of 3.55 Å) to 0.366 at 133° ∠Cu—O—Cu (Cu···Cu distance of 3.4 Å) (Fig. 2E and table S6). A similar result is observed from periodic DFT (table S7). The negative Mulliken charge on the OH decreases abruptly at the spin crossover (Fig. 2F). These changes suggest that the anisotropic bending of the Cu—O—Cu core decreases the population of the O—H bonding orbital, thereby facilitating the proton transfer.

We estimate the geometry of the Cu—O—Cu core at the transition pressure by comparing experimental and computed Raman frequencies. Calculated  $\nu_s(\text{Cu}-\text{O}-\text{Cu})$  and  $\nu_{as}(\text{Cu}-\text{O}-\text{Cu})$  from the fully relaxed  $[\text{Cu}_2\text{OH}]^{3+}$  match the ambient-pressure Raman with  $<\!40\text{-cm}^{-1}$  deviation (fig. S13 and table S8). Using the experimentally calibrated correlation between  $\nu_s(\text{Cu}-\text{O}-\text{Cu})$  and Cu—Cu distance, we estimate the Cu—Cu distance and  $\angle\text{Cu}-\text{O}-\text{Cu}$  angle at 8.5 GPa to be 3.45 Å and 136°, respectively. This geometry is consistent with the periodic DFT-modeled structure at 10 GPa, in reasonable agreement with the experimental transition pressure.

The periodic DFT models reveal a secondary deformation involving the anisotropic distortion of one of the Cu's ligand fields, evident from the N—Cu—O and N—Cu—N bond angles (table S5). The distortion brings one pyridyl nitrogen, labeled N<sub>3</sub>, closer to the bridging oxygen (fig. S14), which serves as the proton receptor.

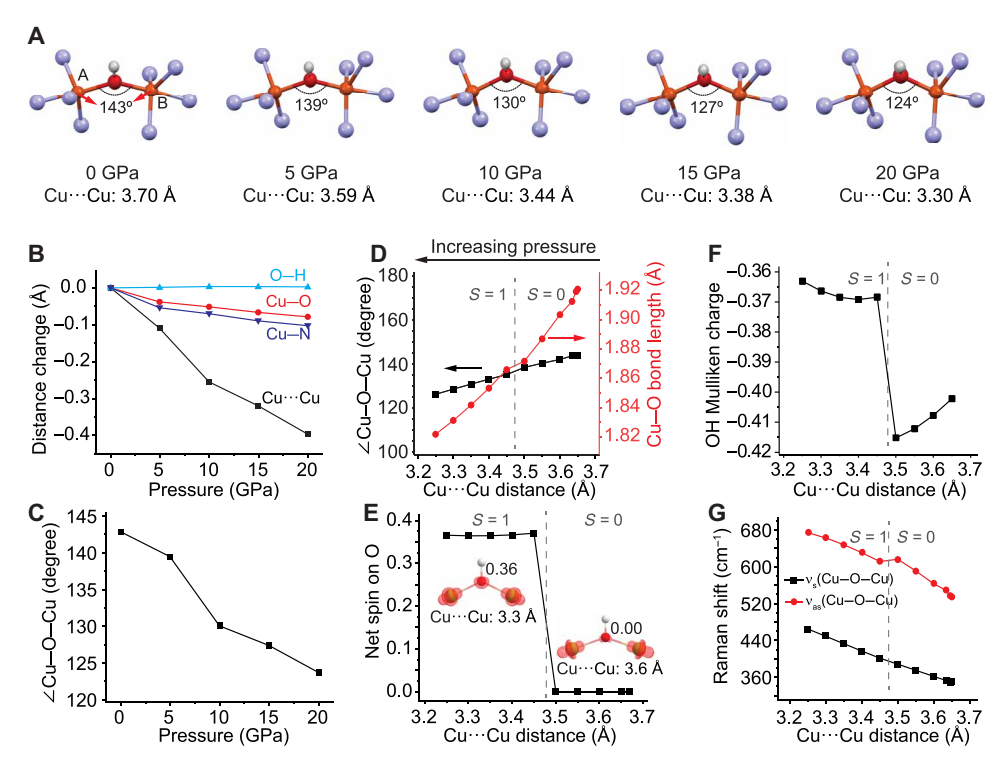


Fig. 2. Formation mechanism of 2. (A) Structure of 1 at different pressures modeled by periodic DFT. Carbon and hydrogen atoms on the TMPA ligands are omitted for clarity. The red arrows denote the primary deformation direction. (B) Relative change of atomic distances with pressure. (C)  $\angle$ Cu-O-Cu as a function of pressure. (D to G) Properties of the truncated  $[Cu_2OH]^{3+}$  model as functions of Cu-Cu distance: (D)  $\angle$ Cu-O-Cu and Cu-O bond length. (E) Net spin on the bridging oxygen. Insets: Spin density isosurfaces at 3.6 Å (right) and 3.3 Å (left) Cu-Cu distances. Isovalue: 0.05. (F) Sum of Mulliken charges on the OH group. (G) Computed Raman shifts of  $\nu_s$ (Cu-O-Cu) and  $\nu_{as}$ (Cu-O-Cu). The vertical dashed lines in (D) to (G) mark the position of the spin crossover.

### **Electronic structure**

The nonequivalent coordination environments of the two coppers induce localized mixed valency. X-ray photoelectric spectroscopy (XPS) of **2** shows split peaks at the Cu 2p levels (Fig. 3A). The  $2p_{3/2}$  peak positions (932.1 and 934.7 eV) correspond to Cu(I) (932.1 to 932.6 eV) and Cu(II) (933.8 to 936.0 eV), respectively (28). Fitting of the peak areas reveals a Cu(I):Cu(II) ratio of 0.94 (table S9). The clearly resolved Cu(I) and Cu(II) features and the close-to-unity ratio suggests localized (Robin-Day type I) mixed valency (29), i.e., a Cu(I)—( $\mu$ -O)—Cu(II) designation. This observation is supported by in situ optical absorption and time-dependent DFT (TD-DFT). Ultraviolet-visible (UV-Vis) spectrum of **1** at ambient pressure (Fig. 3, B and C) is consistent with solution-phase results (23). The two intense bands at 308 and 354 nm are assigned by TD-DFT to the ligand-metal charge transfer (LMCT) from the  $2p_z$  and  $2p_x$  of O to the  $3d_z^2$  of Cu(II) (fig. S15). At 9.6 GPa, the 308-nm band is

obscured by the tail of a higher-energy ligand-centered absorption. The 354-nm band red-shifts to 372 nm and loses intensity (Fig. 3B), coincident with the blue-to-green color change and consistent with the observation that half of the Cu(II) transforms to Cu(I) in the same pressure range. Additional insight into the electronic structure is obtained from the lower-energy absorption (Fig. 3C). The 1-GPa spectrum in the 450- to 1050-nm range is a convolution of three bands at 643, 784, and 921 nm (Fig. 3D, left, and table S10). TD-DFT indicates these bands to be d-d transitions at Cu(II) centers (fig. S16). The convoluted tripeak profile persists up to 8 GPa, with the peaks red-shifting under pressure (fig. S17). At 8.8 GPa, the high-energy edge rises in intensity, resulting in a broad absorption that can be fitted by four peaks (Fig. 3D, right). TD-DFT reproduces the broad absorption profile. The peaks at 705, 784, and 891 nm are identified as d-d transitions. The peak at 616 nm, which gives the high-energy edge, is assigned to the metal-ligand charge transfer

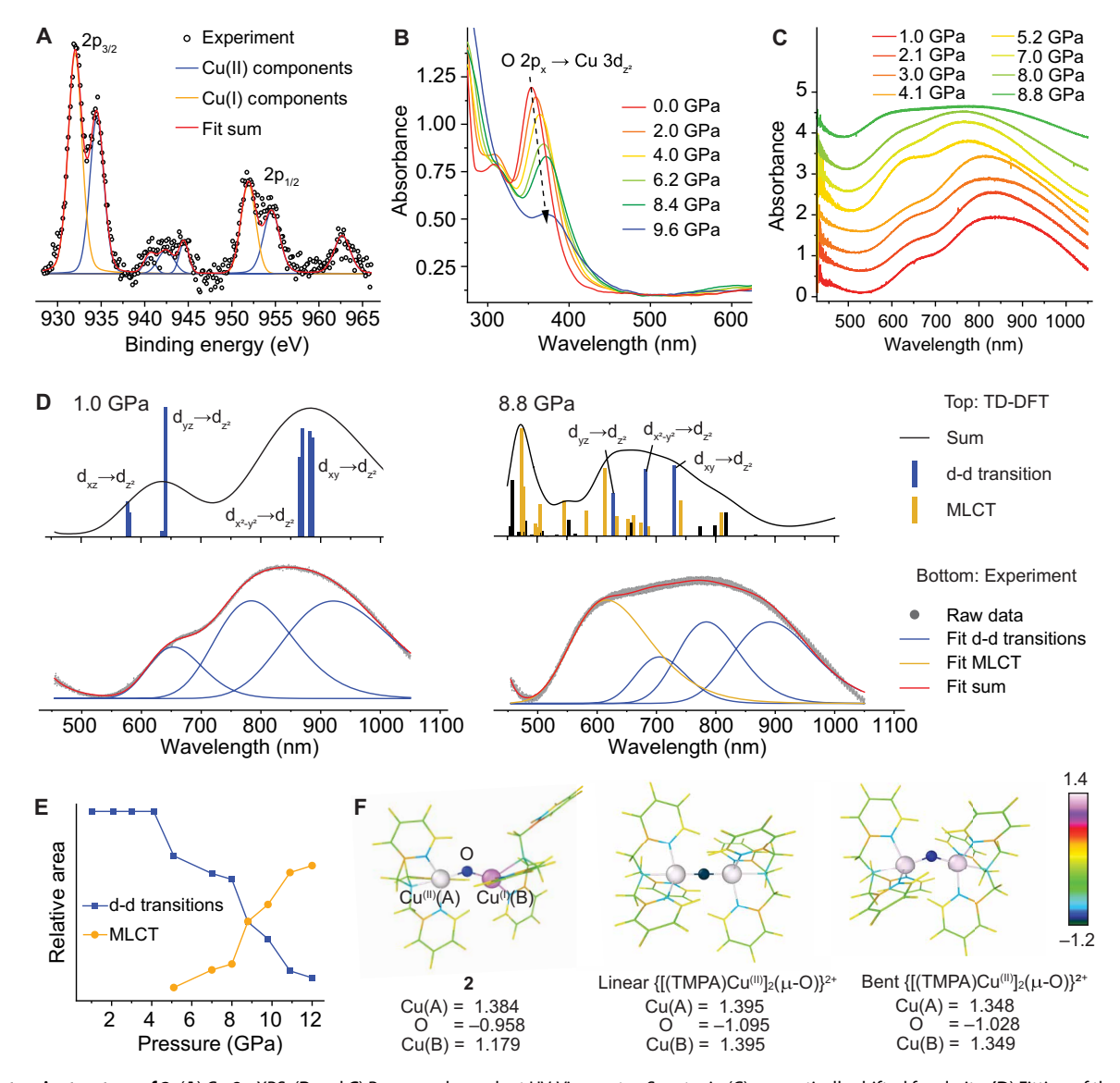


Fig. 3. Electronic structure of 2. (A) Cu-2p XPS. (B and C) Pressure-dependent UV-Vis spectra. Spectra in (C) are vertically shifted for clarity. (D) Fitting of the low-energy UV-Vis spectra (bottom) and TD-DFT-computed spectra (top) at 1.0 and 8.8 GPa. (E) Area sum of d-d transition and MLCT peaks as functions of pressure. (F) Color-coded Mulliken charge distributions.

(MLCT) from the 3d orbitals of Cu(I) to the  $\pi^*$  orbital of the pyridinium (fig. S18). The emergence of the Cu(I)  $\rightarrow$  PyH<sup>+</sup> MLCT, concurrent with the diminished LMCT band in the pressure range of 8–10 GPa (Fig. 3E), supports the formation of Cu(I) in **2**. As the mixed valency is localized, we expect an intervalence charge transfer (IVCT) band to be weak, in contrast to the generally strong absorption in the visible range for intermediate or fully delocalized mixed-valence species (29–31).

The Mulliken charge on the bridging oxygen in 2 is ~12.5% less negative than that in the isoelectronic  $\{[(TPMA)Cu^{(II)}]_2(\mu-O)\}^{2+}$  (Fig. 3F). We further model a bent  $\{[(TPMA)Cu^{(II)}]_2(\mu-O)\}^{2+}$  where  $\angle Cu-O-Cu$  is constrained to 141°, same as in 2. The bending decreases the negative Mulliken charge by ~6%. These results show that both the nonsymmetrical ligand fields and the bending of  $\angle Cu-O-Cu$  contribute to the enhanced electron deficiency of the bridging oxygen in 2. The spin density in 2 is localized on Cu(A) and O, but not on Cu(B) (fig. S19). This is consistent with the localized mixed valency and indicates radical (oxyl) characteristics of the bridging oxygen.

# C-H mono-oxygenation reactivity

We first evaluate the reactivity of **2** in the framework of proton-coupled electron transfer (PCET) by DFT. Using experimentally calibrated references, we calculate the  $pK_a$  (where  $K_a$  is the acid dissociation constant) of protonated **2** (**2H**<sup>+</sup>) to be 25.5 in acetonitrile compared to 23.1 for **1**. The redox potential ( $E^0$ ) of **2** and **2H**<sup>+</sup> is -0.59 and -0.22 V versus  $Fc^0/Fc^+$  (Fc = ferrocene) compared to -1.55 and -0.59 V for {[(TMPA)Cu<sup>(II)</sup>]<sub>2</sub>( $\mu$ -O)}<sup>2+</sup> and **1**, respectively (Fig. 4A). These results show that **2** has simultaneously enhanced proton and electron affinity compared to its symmetrical isoelectronic counterpart, {[(TMPA)Cu<sup>(II)</sup>]<sub>2</sub>( $\mu$ -O)}<sup>2+</sup>. This is in clear contrast to most existing works on engineering the outer ligand sphere of HAA centers, which have revealed a universal compromise between proton and electron affinity (32-36). The O-H bond dissociation energy (BDE) is given by Bordwell's equation (37)

$$BDE_{O-H} = 1.37 \text{ pK}_a + 23.06 E^0 + C_H$$

where  $C_H$  = 59.4 is the experimentally calibrated value for acetonitrile (38), we arrive at BDE<sub>O-H</sub> = 89.2 kcal·mol<sup>-1</sup> for hydrogenated 2 (2H) compared to 77.4 kcal·mol<sup>-1</sup> for one-electron reduced 1 (1<sup>-</sup>). Similarly, we calculate the gas-phase BDE<sub>O-H</sub> to be 91.5 and 77.4 kcal·mol<sup>-1</sup> for 2H and 1<sup>-</sup>, respectively, using phenol dehydrogenation as the probe reaction (fig. S20). These findings highlight the enhanced HAA reactivity of 2 over {[(TMPA)Cu<sup>(II)</sup>]<sub>2</sub>( $\mu$ -O)}<sup>2+</sup>. Bending the  $\angle$ Cu-O-Cu in {[(TMPA)Cu<sup>(II)</sup>]<sub>2</sub>( $\mu$ -O)}<sup>2+</sup> to 141° moderately increases its energy by 3.6 kcal·mol<sup>-1</sup> (fig. S21). The enhanced reactivity of 2 therefore mainly originates from the nonsymmetrical primary ligand sphere and valence localization.

We use 2-butanol, cocrystalized with 1 during synthesis, as the substrate to test the reactivity of 2 after its in situ generation. DFT-modeled reaction pathway (Fig. 4B) shows that HAA from the geminal C—H is mildly downhill by 0.1 kcal·mol<sup>-1</sup>, generating 2H and the 2-hydroxylbutan-2-yl radical. The OH radical then rebounds to the substrate in a predominantly downhill (–95.7 kcal·mol<sup>-1</sup>) step, forming ligand-supported Cu(I) species and the geminal diol that spontaneously condensates to 2-butanone.

Compression of **2** to 12 GPa at room temperature affords a yellow product **3** with strong fluorescence and vanishing  $\nu_s$  (Cu—O—Cu) and  $\nu_{as}$  (Cu—O—Cu) (fig. S22). Cu-2p XPS of the recovered material

yields a Cu(I) to Cu(II) ratio of 2.67, indicating further reduction of the Cu (Fig. 4C). The remaining Cu(II) may originate from incomplete  $2 \rightarrow 3$  transition, or oxidation of Cu(I) species after the sample is recovered from the DAC. In situ UV-Vis spectra (Fig. 4D) show substantially diminished O  $\rightarrow$  Cu LMCT at 15 GPa, consistent with the departure of the bridging oxygen. In the low-energy region, the broadband absorption gains intensity at 600 nm and loses intensity at longer wavelengths upon compression to 13 GPa (Fig. 4E). Fitting of the spectrum combined with TD-DFT shows enhanced Cu  $\rightarrow$  Py and Cu  $\rightarrow$  PyH<sup>+</sup> MLCT together with diminished d-d transitions (Fig. 4F and figs. S17 and S18). The XPS and UV-Vis data support the proposed fate of 2 as TMPA- and TMPAH<sup>+</sup>-bound Cu(I) species.

The recovered product shows a Raman band at 1707 cm<sup>-1</sup> (Fig. 4G), which is assigned to C=O stretching in ketones. When <sup>18</sup>O-labeled **1** is used, this peak splits into two with similar intensity (fig. S23), indicating that half of the ketone oxo originate from the bridging oxygen in **2** and agreeing with the proposed mechanism. Gas chromatographymass spectrometry (GC-MS) provides further identification of the products. Careful analysis of the low-mass region of the MS reveals the presence of species that are not present in **1** (GC integration of 25% relative to TMPA) (Fig. 4H and fig. S24). Fitting of the MS data in this region reveals a mixture of 64.3% 2-butanone, 28.4% 1,3-butanediol, and 7.3% 1,2-butanediol (table S11). The most abundant product corresponds to the oxidation of the weakest C—H (BDE = 91.4 kcal·mol<sup>-1</sup>; Fig. 4H, inset). The **2** also oxidizes 1-octadecene into various alcohol products (fig. S25).

Last, we demonstrate the hydroxylation of methane by 2. Compressing 1 with methane to 13.2 GPa affords a series of color changes from blue to green-brown (Fig. 4, I and J). After releasing the pressure, a liquid is recovered together with the yellow solid 3.  $^{1}$ H–nuclear magnetic resonance of the liquid product in CDCl<sub>3</sub> reveals a peak at  $\delta = 3.49$  parts per million, consistent with the methyl hydrogen in methanol (Fig. 4K). The product contains trace amount of water that obscures the observation of the double splitting or the peak from the hydroxyl group. This result shows that 2 is capable of oxidizing methane with a BDE<sub>C-H</sub> of 105 kcal·mol<sup>-1</sup>.

### **DISCUSSION**

The reactivity of **2** exceeds its symmetrical isoelectronic counterpart,  $\{[(TMPA)Cu]_2 - (\mu-O)\}^{2+}$ , which is shown to oxidize weak H-donors (e.g., 1,4-cyclohexadiene), and is on par with the  $[Cu_2O]^{2+}$  core in Cu-ZSM-5 (9),  $Cu_2@C_3N_4$  (12), and nominal Cu(III) hydroxides (34–36). Note that in both Cu-ZSM-5 and  $Cu_2@C_3N_4$ , appreciable methane oxidation rates have been observed at ambient pressure and 50°C (12). Our reactions take place in the solid or on solid-liquid interfaces under high pressure (39), where diffusion is severely impeded. The additional pressure beyond the formation of **2** is likely needed to bring the substrates close to the  $[Cu_2O]^{2+}$  core to react. It is also possible that further bending of  $\angle Cu-O$ —Cu in **2** enhances its reactivity.

It is intriguing to consider that reactivity toward strong C—H bonds in nature is thought to uniquely occur at mono-copper sites, for example, in particulate methane monooxygenase (pMMO) and lytic polysaccharide monooxygenases. The electronic structure and valence localization of 2 suggest that the contribution of Cu(B) to the HAA reactivity is largely limited to electrostatic effects. Within pMMO, recent studies suggests Cu<sub>D</sub> as the active site (40), with potential for a nearby (5.7 Å) Cu<sub>C</sub> to be occupied simultaneously (41), which could play an analogous role.

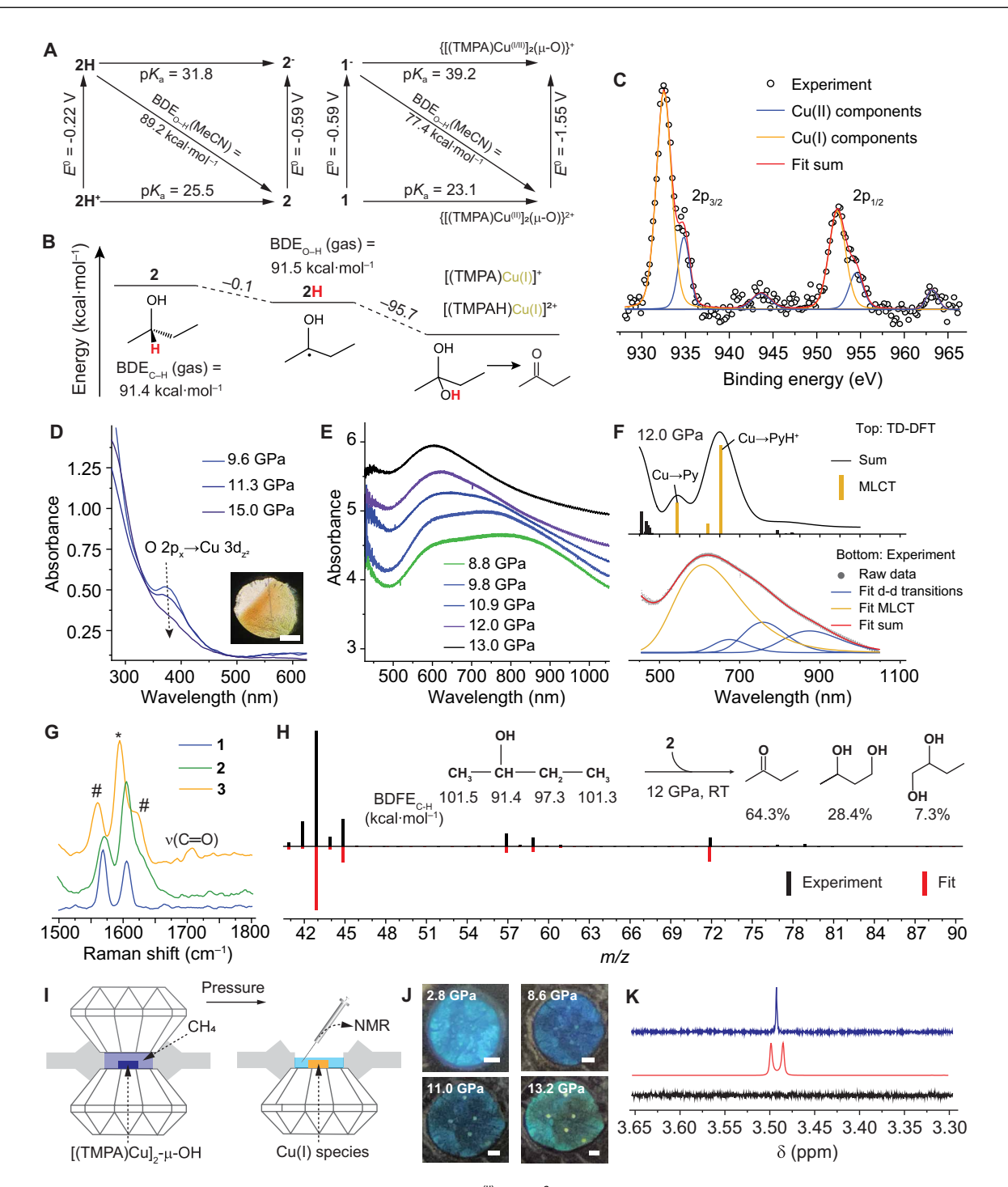


Fig. 4. Reactivity of 2. (A) DFT-computed PCET parameters of 2 and {[(TMPA)Cu<sup>(III)</sup>]<sub>2</sub>(μ-O)]<sup>2+</sup> in acetonitrile. (B) DFT-computed gas-phase reaction energy for the monoxygenation of 2-butanol by 2. Energy levels are not plotted to scale. (C) Cu-2p XPS of recovered 3. (D and E) Pressure-dependent UV-Vis spectra. Inset of (D) shows the optical micrograph of the crystal in the DAC at 12 GPa. Scale bar, 200 μm. Spectra in (E) are vertically shifted for clarity. (F) Fitting of the low-energy spectrum (bottom) and TD-DFT-computed spectrum (top) at 12 GPa. (G) Raman spectra of compounds 1 to 3 at ambient pressure. # and \* mark the peaks from Py and PyH<sup>+</sup>. (H) MS of the liquid product in 3. *m/z*, mass/charge ratio. Inset: Gas-phase BDE of the C—H bonds in 2-butanol, the proposed reaction, and the abundance of the products determined from fitting of the MS. RT, room temperature. (I) Schematic of the high-pressure methane hydroxylation experiment. (J) Optical micrographs of the sample in the DAC. Scale bars, 100 μm. (K) <sup>1</sup>H-NMR of 1 (black), methanol (red), and recovered liquid product after compression (blue). ppm, parts per million.

Precise control of bond scission and formation has been a long sought-after goal in mechanochemistry (42–44), yet most high-pressure reactions found to date involve simultaneous rearrangement of multiple atoms and bonds (21, 45–47). Our results show that hydrostatic pressure drives the transfer of a single proton that can be followed with steady-state spectroscopies. The methodology established here provides a precise tool for the manipulation of molecular structures and properties.

### **MATERIALS AND METHODS**

Compound 1 is synthesized by reacting copper(II) triflate with TMPA and water in the presence of triethylamine, following a previously established procedure (23). High-pressure experiments are carried out in a symmetric DAC (Almax Easylab) using dry silicone oil as the pressure transmitting medium and ruby as the pressure probe (fig. S26). Raman spectra are measured on a confocal microscope-spectrometer using 473-nm laser excitation. UV-Vis spectra are measured on custom-built microfocused spectrometers (fig. S27). Methane is loaded into the DAC by the cryogenic condensation method (fig. S28). DFT computations are carried out at the generalized gradient approximation level of theory for crystal structures, and B3LYP/[6-31g (C, H), 6-311g\* (Cu, O, N)] level of theory for molecular structures. Supplemental Materials and Methods can be found in the Supplementary Materials.

# **Supplementary Materials**

This PDF file includes:

Supplemental Materials and Methods Figs. S1 to S28 Tables S1 to S11 References

## **REFERENCES AND NOTES**

- E. I. Solomon, D. E. Heppner, E. M. Johnston, J. W. Ginsbach, J. Cirera, M. Qayyum, M. T. Kieber-Emmons, C. H. Kjaergaard, R. G. Hadt, L. Tian, Copper active sites in biology. Chem. Rev. 114, 3659–3853 (2014).
- C. Kaintz, S. G. Mauracher, A. Rompel, Type-3 copper proteins: Recent advances on polyphenol oxidases. Adv. Protein Chem. Struct. Biol. 97, 1–35 (2014).
- J. W. Ginsbach, M. T. Kieber-Emmons, R. Nomoto, A. Noguchi, Y. Ohnishi, E. I. Solomon, Structure/function correlations among coupled binuclear copper proteins through spectroscopic and reactivity studies of NspF. Proc. Natl. Acad. Sci. U.S.A. 109, 10793–10797 (2012).
- I. Kipouros, A. Stańczak, J. W. Ginsbach, P. C. Andrikopoulos, L. Rulíšek, E. I. Solomon, Elucidation of the tyrosinase/O<sub>2</sub>/monophenol ternary intermediate that dictates the monooxygenation mechanism in melanin biosynthesis. *Proc. Natl. Acad. Sci. U.S.A.* 119, e2205619119 (2022).
- Y. Matoba, S. Kihara, N. Bando, H. Yoshitsu, M. Sakaguchi, K. Kayama, S. Yanagisawa,
   T. Ogura, M. Sugiyama, Catalytic mechanism of the tyrosinase reaction toward the Tyr98 residue in the caddie protein. *PLoS Biol.* 16, e3000077 (2018).
- P. E. M. Siegbahn, The catalytic cycle of catechol oxidase. J. Biol. Inorg. Chem. 9, 577–590 (2004).
- C. Eicken, B. Krebs, J. C. Sacchettini, Catechol oxidase—structure and activity. Curr. Opin. Struct. Biol. 9, 677–683 (1999).
- C. Gerdemann, C. Eicken, B. Krebs, The crystal structure of catechol oxidase: New insight into the function of type-3 copper proteins. Acc. Chem. Res. 35, 183–191 (2002)
- J. S. Woertink, P. J. Smeets, M. H. Groothaert, M. A. Vance, B. F. Sels, R. A. Schoonheydt, E. I. Solomon, A [Cu<sub>2</sub>O]<sup>2+</sup> core in Cu-ZSM-5, the active site in the oxidation of methane to methanol. *Proc. Natl. Acad. Sci. U.S.A.* **106**, 18908–18913 (2009).
- H. M. Rhoda, D. Plessers, A. J. Heyer, M. L. Bols, R. A. Schoonheydt, B. F. Sels, E. I. Solomon, Spectroscopic definition of a highly reactive site in Cu-CHA for selective methane oxidation: Tuning a mono-μ-oxo dicopper(II) active site for reactivity. J. Am. Chem. Soc. 143, 7531–7540 (2021).

- M. L. Tsai, R. G. Hadt, P. Vanelderen, B. F. Sels, R. A. Schoonheydt, E. I. Solomon, [Cu<sub>2</sub>O]<sup>2+</sup>
   Active site formation in Cu-ZSM-5: Geometric and electronic structure requirements for N<sub>2</sub>O activation. *J. Am. Chem. Soc.* 136, 3522–3529 (2014).
- P. Xie, J. Ding, Z. Yao, T. Pu, P. Zhang, Z. Huang, C. Wang, J. Zhang, N. Zecher-Freeman, H. Zong, D. Yuan, S. Deng, R. Shahbazian-Yassar, C. Wang, Oxo dicopper anchored on carbon nitride for selective oxidation of methane. *Nat. Commun.* 13, 1375 (2022).
- 13. C. Citek, S. Herres-Pawlis, T. D. P. Stack, Low temperature syntheses and reactivity of  $Cu_2O_2$  active-site models. *Acc. Chem. Res.* **48**, 2424–2433 (2015).
- H. V. Obias, Y. Lin, N. N. Murthy, E. Pidcock, E. I. Solomon, M. Ralle, N. J. Blackburn, Y.-M. Neuhold, A. D. Zuberbühler, K. D. Karlin, Peroxo-, oxo-, and hydroxo-bridged dicopper complexes: Observation of exogenous hydrocarbon substrate oxidation. *J. Am. Chem. Soc.* 120, 12960–12961 (1998).
- R. Jurgeleit, B. Grimm-Lebsanft, B. M. Flöser, M. Teubner, S. Buchenau, L. Senft,
  J. Hoffmann, M. Naumova, C. Näther, I. Ivanović-Burmazović, M. Rübhausen, F. Tuczek,
  Catalytic oxygenation of hydrocarbons by mono-μ-oxo dicopper(II) species resulting
  from O-O cleavage of tetranuclear Cu<sup>I</sup>/Cu<sup>II</sup> peroxo complexes. *Angew. Chemie Int. Ed.* 60,
  14154–14162 (2021).
- P. Haack, C. Limberg, Molecular Cu<sup>II</sup>-O-Cu<sup>II</sup> complexes: Still waters run deep. Angew. Chemie Int. Ed. 53, 4282–4293 (2014).
- P. Haack, A. Kärgel, C. Greco, J. Dokic, B. Braun, F. F. Pfaff, S. Mebs, K. Ray, C. Limberg, Access to a Cu<sup>II</sup>-O-Cu<sup>II</sup> motif: Spectroscopic properties, solution structure, and reactivity. J. Am. Chem. Soc. 135, 16148–16160 (2013).
- T. Kayatani, Y. Hayashi, M. Suzuki, K. Inomata, A. Uehara, Coordination asymmetry of a dinuclear copper(II) complex: Synthesis, structure, and magnetism. *Bull. Chem. Soc. Jpn.* 69, 389–397 (1996).
- C. Fernandes, A. Neves, A. J. Bortoluzzi, A. S. Mangrich, E. Rentschler, B. Szpoganicz, E. Schwingel, A new dinuclear unsymmetric copper(II) complex as model for the active site of catechol oxidase. *Inorganica Chim. Acta* 320, 12–21 (2001).
- B. M. T. Lam, J. A. Halfen, V. G. Young Jr., J. R. Hagadorn, P. L. Holland, A. Lledós,
   L. Cucurull-Sánchez, J. J. Novoa, S. Alvarez, W. B. Tolman, Ligand macrocycle structural effects on copper-dioxygen reactivity. *Inorg. Chem.* 39, 4059–4072 (2000).
- H. Yan, F. Yang, D. Pan, Y. Lin, J. N. Hohman, D. Solis-Ibarra, F. H. Li, J. E. P. Dahl, R. M. K. Carlson, B. A. Tkachenko, A. A. Fokin, P. R. Schreiner, G. Galli, W. L. Mao, Z.-X. Shen, N. A. Melosh, Sterically controlled mechanochemistry under hydrostatic pressure. *Nature* 554, 505–510 (2018).
- Z. Lu, C. M. Archambault, S. Li, U. Syed, S. Wang, A. Kumar, G. Shen, Z. Liu, M. A. Omary, H. Yan, Modulating the extent of anisotropic cuprophilicity via high pressure with piezochromic luminescence sensitization. *J. Phys. Chem. Lett.* 14, 508–515 (2023).
- G. Ali, P. E. VanNatta, D. A. Ramirez, K. M. Light, M. T. Kieber-Emmons, Thermodynamics of a μ-oxo dicopper(II) complex for hydrogen atom abstraction. *J. Am. Chem. Soc.* 139, 18448–18451 (2017).
- P. E. VanNatta, D. A. Ramirez, A. R. Velarde, G. Ali, M. T. Kieber-Emmons, Exceptionally high
  O-H bond dissociation free energy of a dicopper(II) μ-hydroxo complex and insights into
  the geometric and electronic structure origins thereof. *J. Am. Chem. Soc.* 142,
  16292–16312 (2020).
- N. Wattanavichean, E. Casey, R. J. Nichols, H. Arnolds, Discrimination between hydrogen bonding and protonation in the spectra of a surface-enhanced Raman sensor. *Phys. Chem. Chem. Phys.* 20, 866–871 (2018).
- S. Scheiner, Calculation of isotope effects from first principles. Biochim. Biophys. Acta - Bioenerg. 1458, 28–42 (2000).
- J. P. Perdew, K. Burke, M. Ernzerhof, Generalized gradient approximation made simple. *Phys. Rev. Lett.* 77, 3865–3868 (1996).
- M. C. Biesinger, Advanced analysis of copper X-ray photoelectron spectra. Surf. Interface Anal. 49, 1325–1334 (2017).
- M. B. Robin, P. Day, Mixed valence chemistry-A survey and classification. Adv. Inorg. Chem. Radiochem. 10, 247–422 (1968).
- J. Li, R. Matheu, F. Ke, Z. Liu, Y. Lin, H. I. Karunadasa, Mosaic Cu<sup>I</sup>—Cu<sup>II</sup>—In<sup>III</sup> 2D perovskites: Pressure-dependence of the intervalence charge transfer and a mechanochemical alloying method. *Angew. Chemie Int. Ed.* 62, e202300957 (2023).
- B. S. Brunschwig, C. Creutz, N. Sutin, Optical transitions of symmetrical mixed-valence systems in the Class II-III regime. Chem. Soc. Rev. 31, 168–184 (2002).
- D. Usharani, D. C. Lacy, A. S. Borovik, S. Shaik, Dichotomous hydrogen atom transfer vs proton-coupled electron transfer during activation of X-H bonds (X = C, N, O) by nonheme iron-oxo complexes of variable basicity. J. Am. Chem. Soc. 135, 17090-17104 (2012)
- R. Gupta, A. S. Borovik, Monomeric Mn<sup>III/II</sup> and Fe<sup>III/II</sup> complexes with terminal hydroxo and oxo ligands: probing reactivity via O–H bond dissociation energies. *J. Am. Chem. Soc.* 125, 13234–13242 (2003).
- D. Dhar, W. B. Tolman, Hydrogen atom abstraction from hydrocarbons by a copper(III)hydroxide complex. J. Am. Chem. Soc. 137, 1322–1329 (2015).
- D. Dhar, G. M. Yee, W. B. Tolman, Effects of charged ligand substituents on the properties of the formally copper(III)-hydroxide ([CuOH]<sup>2+</sup>) unit. *Inorg. Chem.* 57, 9794–9806 (2018).

# SCIENCE ADVANCES | RESEARCH ARTICLE

- D. Dhar, G. M. Yee, A. D. Spaeth, D. W. Boyce, H. Zhang, B. Dereli, C. J. Cramer, W. B. Tolman, Perturbing the copper(III)-hydroxide unit through ligand structural variation. *J. Am. Chem. Soc.* 138, 356–368 (2016).
- F. G. Bordwell, Equilibrium acidities in dimethyl sulfoxide solution. Acc. Chem. Res. 21, 456–463 (1988).
- J. J. Warren, T. A. Tronic, J. M. Mayer, Thermochemistry of proton-coupled electron transfer reagents and its implications. Chem. Rev. 110, 6961–7001 (2010).
- A. Würflinger, L. C. Pardo, Thermodynamic measurements on CH<sub>3</sub>CCl<sub>3</sub>, (CH<sub>3</sub>)<sub>2</sub>CBr<sub>2</sub>, and on nC<sub>20</sub>H<sub>42</sub> at high pressures. Z. Naturforsch. A 57, 177–183 (2002).
- F. J. Tuci, R. J. Jodts, B. M. Hoffman, A. C. Rosenzweig, Product analogue binding identifies the copper active site of particulate methane monooxygenase. *Nat. Catal.* 6, 1194–1204 (2023)
- F. J. Tucci, A. C. Rosenzweig, Direct methane oxidation by copper- and iron-dependent methane monooxygenases. Chem. Rev. 124, 1288–1320 (2024).
- G. Boendgen, P. Saalfrank, STM-induced desorption of hydrogen from a silicon surface: An open-system density matrix study. J. Phys. Chem. B 102, 8029–8035 (1998).
- 43. J. Liang, J. M. Fernández, Mechanochemistry: One bond at a time. ACS Nano 3, 1628–1645
- L. Chen, J. Wen, P. Zhang, B. Yu, C. Chen, T. Ma, X. Lu, S. H. Kim, L. Qian, Nanomanufacturing of silicon surface with a single atomic layer precision via mechanochemical reactions. *Nat. Commun.* 9, 1542 (2018).
- D. Gao, X. Tang, J. Xu, X. Yang, P. Zhang, G. Che, Y. Wang, Y. Chen, X. Gao, X. Dong, H. Zheng, K. Li, H.-K. Mao, Crystalline C<sub>3</sub>N<sub>3</sub>H<sub>3</sub> tube (3,0) nanothreads. *Proc. Natl. Acad. Sci. U.S.A.* 119, e2201165119 (2022).
- F. Ke, C. Wang, C. Jia, N. R. Wolf, J. Yan, S. Niu, T. P. Devereaux, H. I. Karunadasa, W. L. Mao, Y. Lin, Preserving a robust CsPbl<sub>3</sub> perovskite phase via pressure-directed octahedral tilt. Nat. Commun. 12, 461 (2021).
- S. G. Dunning, L. Zhu, B. Chen, S. Chariton, V. B. Prakapenka, M. Somayazulu, T. A. Strobel, Solid-state pathway control via reaction-directing heteroatoms: Ordered pyridazine nanothreads through selective cycloaddition. J. Am. Chem. Soc. 144, 2073–2078 (2022).
- 48. CrysAlisPRO-Oxford Diffraction (Agilent Technologies UK Ltd).
- SCALE3 ABSPACK-An Oxford Diffraction program (1.0.4, gui:1.0.3) (Oxford Diffraction Ltd, 2005).
- G. M. Sheldrick, SHELXT-Integrated space-group and crystal-structure determination. Acta Crystallogr. A 71, 3–8 (2015).
- O. V. Dolomanov, L. J. Bourhis, R. J. Gildea, J. A. K. Howard, H. Puschmann, OLEX2: A complete structure solution, refinement and analysis program. *J. Appl. Cryst.* 42, 339–341 (2000)
- H.-K. Mao, W. L. Mao, Theory and practice—Diamond-anvil cells and probes for high P-T mineral physics studies, in *Treatise on Geophysics* (Elsevier, 2007), vol. 2, pp. 231-267.
- P. I. Dorogokupets, A. R. Oganov, Ruby, metals, and MgO as alternative pressure scales: A semiempirical description of shock-wave, ultrasonic, x-ray, and thermochemical data at high temperatures and pressures. *Phys. Rev. B. Condens. Matter Mater. Phys.* 75, 024115 (2007).
- P. Hartmann, C. L. Bender, J. Sann, A. K. Dürr, M. Jansen, J. Janek, P. Adelhelm, A comprehensive study on the cell chemistry of the sodium superoxide (NaO<sub>2</sub>) battery. *Phys. Chem. Chem. Phys.* 15, 11661–11672 (2013).
- S. Stein, Mass spectral reference libraries: An ever-expanding resource for chemical identification. Anal. Chem. 84, 7274–7282 (2012).
- 56. P. E. Blöchl, Projector augmented-wave method. Phys. Rev. B 50, 17953–17979 (1994).
- P. Giannozzi, S. Baroni, N. Bonini, M. Calandra, R. Car, C. Cavazzoni, D. Ceresoli, G. L. Chiarotti, M. Cococcioni, I. Dabo, A. D. Corso, S. de Gironcoli, S. Fabris, G. Fratesi, R. Gebauer, U. Gerstmann, C. Gougoussis, A. Kokalj, M. Lazzeri, L. Martin-Samos, N. Marzari, F. Mauri, R. Mazzarello, S. Paolini, A. Pasquarello, L. Paulatto, C. Sbraccia, S. Scandolo, G. Sclauzero, A. P. Seitsonen, A. Smogunov, P. Umaril, R. M. Wentzcovitch, QUANTUM ESPRESSO: A modular and open-source software project for quantum simulations of materials. J. Phys. Condens. Matter 21, 395502 (2009).
- L. Wang, T. Maxisch, G. Ceder, Oxidation energies of transition metal oxides within the GGA+U framework. *Phys. Rev. B* 73, 195107 (2006).
- G. W. Mann, K. Lee, M. Cococcioni, B. Smit, J. B. Neaton, First-principles Hubbard U approach for small molecule binding in metal-organic frameworks. J. Chem. Phys. 144, 174104 (2016).
- S. Grimme, J. Antony, S. Ehrlich, H. Krieg, A consistent and accurate ab initio parametrization of density functional dispersion correction (DFT-D) for the 94 elements H-Pu. J. Chem. Phys. 132, 154104 (2010).
- S. H. Vosko, L. Wilk, M. Nusair, Accurate spin-dependent electron liquid correlation energies for local spin density calculations: a critical analysis. Can. J. Phys. 58, 1200–1211 (1980)
- R. Krishnan, J. S. Binkley, R. Seeger, J. A. Pople, Self-consistent molecular orbital methods. XX. A basis set for correlated wave functions. J. Chem. Phys. 72, 650–654 (2008).

- A. J. H. Wachters, A. J. H., Gaussian basis set for molecular wavefunctions containing thirdrow atoms. J. Chem. Phys. 52, 1033–1036 (2003).
- W. J. Hehre, R. Ditchfield, J. A. Pople, Self-consistent molecular orbital methods. XII.
   Further extensions of gaussian—type basis sets for use in molecular orbital studies of organic molecules. J. Chem. Phys. 56, 2257–2261 (2003).
- R. Ditchfield, W. J. Hehre, J. A. Pople, Self-consistent molecular-orbital methods. IX. An extended gaussian-type basis for molecular-orbital studies of organic molecules. *J. Chem. Phys.* 54, 724–728 (2003).
- K. Raghavachari, G. W. Trucks, Highly correlated systems. Excitation energies of first row transition metals Sc–Cu. J. Chem. Phys. 91, 1062–1065 (1989).
- P. J. Hay, Gaussian basis sets for molecular calculations. The representation of 3d orbitals in transition-metal atoms. J. Chem. Phys. 66, 4377–4384 (2008).
- P. J. Stephens, F. J. Devlin, C. F. Chabalowski, M. J. Frisch, Ab initio calculation of vibrational absorption and circular dichroism spectra using density functional force fields. *J. Phys. Chem.* 98, 11623–11627 (1994).
- C. Lee, W. Yang, R. G. Parr, Development of the Colle-Salvetti correlation-energy formula into a functional of the electron density. *Phys. Rev. B* 37, 785–789 (1988).
- A. D. Becke, Density-functional thermochemistry. III. The role of exact exchange. J. Chem. Phys. 98, 5648–5652 (1993).
- F. Neese, F. Wennmohs, U. Becker, C. Riplinger, The ORCA quantum chemistry program package. J. Chem. Phys. 152, 224108 (2020).
- C. P. Kelly, C. J. Cramer, D. G. Truhlar, Single-ion solvation free energies and the normal hydrogen electrode potential in methanol, acetonitrile, and dimethyl sulfoxide. *J. Phys. Chem. B* 111, 408–422 (2007).
- E. Rossini, E.-W. Knapp, Proton solvation in protic and aprotic solvents. *J. Comput. Chem.* 37, 1082–1091 (2016).
- D. O. Kashinski, G. M. Chase, R. G. Nelson, O. E. Di Nallo, A. N. Scales, D. L. VanderLey, E. F. C. Byrd, Harmonic vibrational frequencies: Approximate global scaling factors for TPSS, M06, and M11 functional families using several common basis sets. *J. Phys. Chem. A* 121, 2265–2273 (2017).
- C. F. Macrae, P. R. Edgington, P. McCabe, E. Pidcock, G. P. Shields, R. Taylor, M. T. J. van de Streek, Mercury: Visualization and analysis of crystal structures. J. Appl. Cryst. 39, 453–457 (2006).
- K. Momma, F. Izumi, VESTA 3 for three-dimensional visualization of crystal, volumetric and morphology data. J. Appl. Cryst. 44, 1272–1276 (2011).
- Chemcraft–Graphical software for visualization of quantum chemistry computations version 1.8, build 682; https://chemcraftprog.com.
- B. Ruscic, Active thermochemical tables: Sequential bond dissociation enthalpies of methane, ethane, and methanol and the related thermochemistry. J. Phys. Chem. A 119, 7810–7837 (2015).
- M. Byrn, M. Calvin, Oxygen-18 exchange reactions of aldehydes and ketones. J. Am. Chem. Soc. 88, 1916–1922 (1966).
- S. Klotz, J. C. Chervin, P. Munsch, G. Le Marchand, Hydrostatic limits of 11 pressure transmitting media. J. Phys. D Appl. Phys. 42, 075413 (2009).

Acknowledgments: We thank V. Nesterov, S. Sepulveda, K. Smart, S. Ma, H. Wang, and T. Cundari for the help with experiments and discussion. Funding: This research used resources of the National Synchrotron Light Source II, a U.S. Department of Energy (DOE) Office of Science User Facility operated for the DOE Office of Science by Brookhaven National Laboratory under contract no. DE-SC0012704. Use of the 22-IR-1 beamline is supported by the National Science Foundation Division of Earth Sciences (EAR) SEES: Synchrotron Earth and Environmental Science (EAR-2223273) and Chicago/DOE Alliance Center (CDAC) DE-NA0003975. Part of this work was performed on Cruntch, the high-performance computing cluster at University of North Texas supported by the NSF-MRI grants CHE-1531468 and OAC-2117247. This work was performed in part at the University of North Texas's Materials Research Facility, a shared research facility for multidimensional fabrication and characterization. J.D. and N.J.M.'s works were supported by the NSF-REU grant CHE-1757946. Author contributions: Conceptualization: P.E.V. and H.Y. Methodology: P.E.V., H.Y., K.W., and Z.L. Investigation: P.E.V., C.M.A., S.W., T.L., N.J.M., and S.K.W. Instrumentation design and fabrication: P.E.V., Z.L., and H.Y. Funding acquisition: H.Y. DFT studies: P.E.V., J.D., and H.Y. Data analysis: P.E.V., M.T.K.-E., and H.Y. Writing—original draft: P.E.V., M.T.K.-E, and H.Y. Writingreview and editing: P.E.V., C.M.A., S.W., T.L., J.D., N.J.M., S.K.W., K.W., Z.L., M.T.K.-E., and H.Y. Competing interests: The authors declare that they have no competing interest. Data and materials availability: All data needed to evaluate the conclusions in this paper are present in the paper and/or the Supplementary Materials.

Submitted 8 May 2024 Accepted 29 August 2024 Published 4 October 2024 10.1126/sciadv.adq3366